



Quantitative measure of correlation strength among intertwined many-body interactions

Hideaki Iwasawa ^{1,2,3,4,*} Tetsuro Ueno,^{2,3,5} Yoshiyuki Yoshida,⁶ Hiroshi Eisaki,⁶ Yoshihiro Aiura,^{6,†} and Kenya Shimada ⁴

¹*Institute for Advanced Synchrotron Light Source, National Institutes for Quantum Science and Technology, Sendai 980-8579, Japan*

²*Synchrotron Radiation Research Center, National Institutes for Quantum Science and Technology, Hyogo 679-5148, Japan*

³*QST Advanced Study Laboratory, National Institutes for Quantum Science and Technology, Chiba 263-8555, Japan*

⁴*Hiroshima Synchrotron Radiation Center, Hiroshima University, Hiroshima 739-0046, Japan*

⁵*Quantum Materials and Applications Research Center, National Institutes for Quantum Science and Technology, Gunma 370-1292, Japan*

⁶*Electronics and Photonics Research Institute, National Institute of Advanced Industrial Science and Technology, Ibaraki 305-8568, Japan*



(Received 16 June 2023; accepted 1 September 2023; published 20 December 2023)

The intertwined coupling among various many-body interactions is increasingly recognized as playing a key role in strongly correlated electron systems. However, understanding their relationship to physical properties is challenging due to the lack of a definitive experimental measure. Here, we report an analytical approach that utilizes machine learning to enable a higher level of evaluation of many-body interactions through a large amount of data from a single material using spatially resolved and angle-resolved photoemission spectroscopy. We demonstrate that various physical parameters, including the coupling strengths of electron-electron and electron-boson interactions, can be statistically evaluated, and the correlation between many-body interactions can also be accessed. Our approach thus provides a quantitative measure of the microscopic variables and serves as a linking bridge between them, holding great promise in disentangling the complex nature of strongly correlated materials where many-body interactions generally mutually interplay.

DOI: [10.1103/PhysRevResearch.5.043266](https://doi.org/10.1103/PhysRevResearch.5.043266)

I. INTRODUCTION

Many-body interactions are critical for predicting and designing materials with desired properties, as well as for exploring new quantum phenomena [1]. In strongly correlated electron systems, the interplay among various types of many-body interactions is considered particularly important. A representative example of such systems is high-critical-temperature (high- T_c) cuprate superconductors. In these materials, the electron-electron interactions are fundamental for understanding their complex quantum phases, as various quantum orders, including superconducting states, emerge through doping carriers into the Mott insulator [2]. On the other hand, despite many reports of the electron-phonon interactions coupling to the electronic states strongly in the high- T_c cuprate superconductors [3–6], it has been generally considered skeptical whether the electron-phonon interactions play a leading role in high- T_c cuprates. In contrast, it has been suggested that the electron-phonon interactions contribute to the high- T_c superconductivity in a different role, such as the cooperative interplay between electron-electron interactions [7–10] as well as multichannel superconductivity [11–13], beyond their canonical role for the formation of

the Cooper pairs in low-temperature superconductors [14]. However, discussions on the interplay among intertwined interactions have been limited to a qualitative level due to the lack of established experimental scales for determining the numerical and quantitative strength of such interactions. Here, we present a quantitative measure of the correlation among physical parameters and many-body interactions in high- T_c cuprate superconductors by utilizing spatially resolved and angle-resolved photoemission spectroscopy (ARPES) with the help of machine learning-based analysis. Our analytical approach has broad applicability to various systems, providing a different perspective on uncovering the physical properties of materials through the quantitative evaluation of physical parameters, many-body interactions, and their correlation.

II. METHODS

In this study, we analyzed the spatial mapping data set of fine electronic states from the overdoped Bi-based high- T_c cuprate $\text{Bi}_2\text{Sr}_2\text{CaCu}_2\text{O}_{8+\delta}$ (Bi2212). High-quality overdoped Bi2212 ($T_c = 75$ K) single crystals were prepared by the traveling-solvent floating-zone techniques [15]. Spatially resolved ARPES experiments were performed at the ultrahigh-resolution laser micro-ARPES system of the Hiroshima Synchrotron Radiation Center (HiSOR) [16] using a photon energy of 6.36 eV at 12.5 K. All the data were measured by a high-resolution hemispherical electron analyzer (R4000, Scienta) after cleaving the samples *in situ* in an ultrahigh vacuum better than 5×10^{-11} Torr at 12.5 K. The energy, angular, and spatial resolution were better than 3 meV, 0.05° , and 5 μm , respectively.

*iwasawa.hideaki@qst.go.jp

†Present address: TIA central office, National Institute of Advanced Industrial Science and Technology, Ibaraki 305-8568, Japan.

Published by the American Physical Society under the terms of the [Creative Commons Attribution 4.0 International](https://creativecommons.org/licenses/by/4.0/) license. Further distribution of this work must maintain attribution to the author(s) and the published article's title, journal citation, and DOI.

For the statistical analysis of the extracted physical parameters, we calculated the Pearson correlation coefficient and p value using Python's `scipy.stats.pearsonr` function from the `SCIPY` package [17]. Additionally, we utilized K -means clustering, an unsupervised learning technique, which is valuable for categorizing spatially resolved ARPES data sets, as we have previously demonstrated [18].

The Pearson correlation coefficient is a statistical measure that quantifies the strength and direction of the linear relationship between two continuous variables [19]. The coefficient (r) ranges from -1 to $+1$, where $+1$ indicates a perfectly positive correlation (as one variable increases, the other increases), while -1 indicates a perfectly negative correlation (as one variable increases, the other decreases), and 0 indicates no correlation between the two variables.

The Pearson correlation coefficient is calculated by dividing the covariance of the two variables by the product of their standard deviations, as follows:

$$r_{xy} = \frac{\sum_{i=1}^n (x_i - \bar{x})(y_i - \bar{y})}{\sqrt{\sum_{i=1}^n (x_i - \bar{x})^2} \sqrt{\sum_{i=1}^n (y_i - \bar{y})^2}}, \quad (1)$$

where x and y are the two variables, and \bar{x} and \bar{y} are their mean values.

The p value is a measure of the statistical significance of the Pearson correlation coefficient. It indicates the probability of obtaining the observed correlation coefficient or a more extreme value by chance, assuming that there is no real correlation between the two variables. A p value less than 0.05 is generally considered statistically significant, meaning that there is less than a 5% chance that the observed correlation occurred by chance. We calculated the p value via a t test. The t value is calculated by dividing the Pearson correlation coefficient by its standard error, which is estimated based on the sample size and the degrees of freedom ($n - 2$). The t value is then compared to the t distribution with ($n - 2$) degrees of freedom to obtain the p value.

III. RESULTS AND DISCUSSION

A. Experimental and analytical overview

Figure 1 illustrates our experimental and analytical approach based on the spatially resolved ARPES experiment conducted on the overdoped Bi2212. First, it should be mentioned that the compatibility of high-quality energy, momentum, and spatial resolutions is indispensable in our approach. This is achieved by using our laser-based micro-ARPES system [16]. The spatial mapping was performed with the configurations depicted in Figs. 1(a) and 1(b), where the sample was rotated 35° from the normal of the electron analyzer to observe the electronic states crossing the Fermi level (E_F) along the nodal direction $[(0,0)-(\pi,\pi)]$. This means that the laser was incident on the sample at an angle close to the sample normal, with an offset of 10° . We employed s polarization, which is required to observe the Cu $3d_{x^2-y^2}$ band in terms of the selection rule [20], whereas only the antibonding band can be observed from the bilayer-split CuO conduction bands for low-energy photons (6.36 eV in the present case) [5,21].

As shown in Fig. 1(c), the spatial mapping of the overall sample surface demonstrates that a relatively large (order of

mm) portion of the cleaved surface has a rather homogeneous intensity distribution. Each pixel denotes a fully integrated intensity of a two-dimensional ARPES image $I_{\text{ARPES}}(\mathbf{k}, \omega)$, similar to Fig. 1(e), in energy and angle dimensions. We then selected one pixel ($100 \times 100 \mu\text{m}^2$), as indicated by the white box in Fig. 1(c), and performed high-resolution and finer spatial mapping, as shown in Fig. 1(d), with vertical and horizontal steps of $5 \mu\text{m}$ while maintaining a high resolution of better than 3 meV. Figure 1(e) shows a raw ARPES image at one pixel in Fig. 1(d), presenting a sharp quasiparticle dispersion that withstands a detailed spectral line-shape analysis shown in Figs. 1(f)–1(h). Despite a short acquisition time of 5 s, a signal-to-noise (SN) ratio is adequately high, as evidenced by the raw MDCs along with their fitting curves in Fig. 1(f) (also refer to Supplemental Material Note 1 and Supplemental Material Fig. S1 [22]). It should be noted that the purpose of the short acquisition time is to reduce the total measurement time and thus suppress extrinsic effects, such as spatial and temporal changes of spectra.

We performed spectral line-shape analysis on the momentum distribution curves (MDCs) at constant energy, which is conventionally accepted for evaluating many-body interactions [23,24]. Fig. 1(f) displays MDCs at various energies, which were well fitted by a simple Lorentzian function. This enabled us to determine the energy dependence of the peak intensity, position, and width [$I_{\text{MDC}}(\omega)$, $\varepsilon_k(\omega)$, and $\Delta k(\omega)$], as shown in Fig. 1(g). Further analysis of such peak information can provide valuable information, such as the carrier density, effective mass, and lifetime, about the electronic structure, which is deeply related to the physical properties of a material.

To characterize the multiple types of coupling parameters, such as electron-electron interaction (λ_{ee}), electron-boson interaction (λ_{eb}), and the sum of all interactions (λ_{tot}), we determined various velocities by fitting the band dispersion at different energy regions [left panel of Fig. 1(h)]. We evaluated the band renormalization by referencing the velocity of the noninteracting band (v_0), also known as the bare band. Namely, the Fermi velocity (v_F), reflecting all interactions, was used as a measure of the sum of all interactions, such that $\lambda_{\text{tot}} = v_0/v_F - 1$. Similarly, the group velocity at the higher energy region (v_h), reflecting the electron-electron interaction, was used for examining the electron-electron interaction, such that $\lambda_{ee} = v_0/v_h - 1$. As for the electron-boson interaction, we simplified our focus on the most prominent kink in the dispersion around 70 meV, although multiple kinks have been reported in Bi2212 systems [6,25,26]. We labeled this kink as α following the notation used in Ref. [6]. The coupling parameter of the α kink can then be given by the ratio of group velocities ($\lambda_{eb} = v_{\text{HE}}^\alpha/v_{\text{LE}}^\alpha - 1$) at lower and higher energy regions with respect to the kink energy. It should be noted that the constant bare velocity ($v_0 = 4.0$ eVÅ) was employed here for simplicity because the analysis with a parametrized bare velocity did not bring essential differences (see Supplemental Material Note 2 and Supplemental Material Figs. 7–10 [22]). All the parameters shown in this paper were obtained by following the abovementioned procedure. The fitting ranges used for deducing the velocities are the following: 0.00 to -0.02 eV for v_F , -0.10 to -0.14 eV for v_h , -0.045 to -0.075 eV for v_{LE}^α , and -0.075 to -0.125 eV for v_{HE}^α .

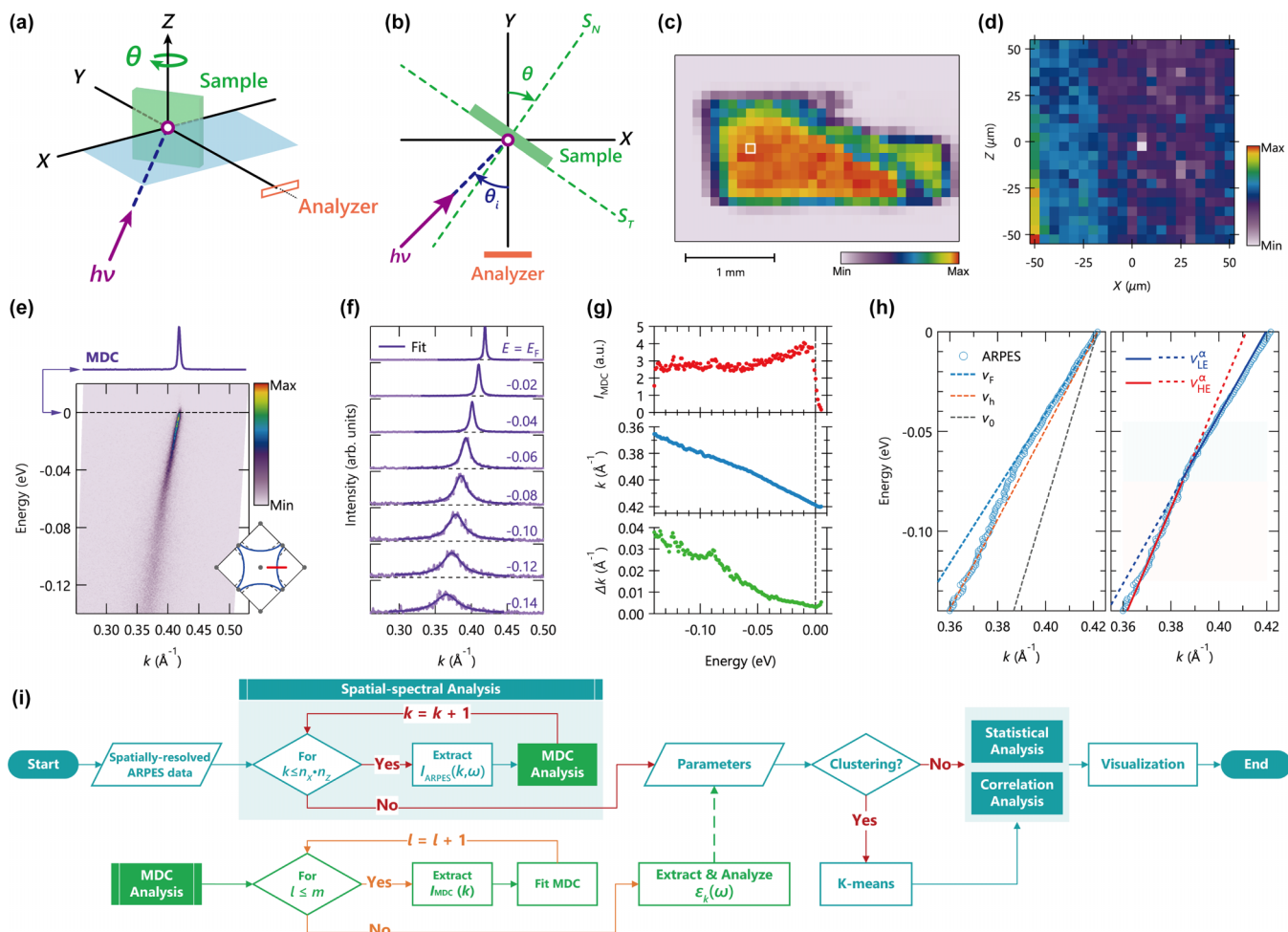


FIG. 1. General overview of spatially resolved ARPES experiment and spectral line-shape analysis. (a), (b) Schematic drawings of the experimental layout for present spatially resolved ARPES experiments in an aerial and top view, respectively. The laser light source is incident at 45° with respect to the electron analyzer. (c), (d) Total ARPES intensity mapping in the real space for overall and local regions, respectively. The area of (d) is shown by a white box in (c). (e) Exemplary ARPES image at one pixel ($5 \times 5 \mu\text{m}^2$) from the spatial ARPES mapping data set, shown in (d). The inset shows the schematic Fermi surface, where the measured location along the nodal direction is indicated by the red line. (f) Multiple MDCs at various energies, extracted from (e), where the fit curves (solid lines) are overlaid. (g) The energy dependence of the intensity, position, and width of the MDC peak, obtained from the curve fitting. (h) Determination of (left) the Fermi velocity (v_F) and group velocity at high energy region (v_h), compared with the bare velocity (v_0), and (right) the coupling parameter of the kink (α), given by the ratio of group velocities at low and high energy regions (v_{LE}^α and v_{HE}^α). (i) Flow chart of the spatial spectral analysis and the subsequent statistical and correlation analysis.

Figure 1(i) shows a flow chart illustrating the overall analysis procedure for our spatial spectral analysis. In this analysis, we extended the MDC analysis at a spatial coordinate (X_i, Z_j) to all the spatial mapping data [Fig. 1(d)]. Here, i and j are integers representing acquisition points along the X and Z axis, respectively, ranging from 1 to $n_x (=21)$ and $n_z (=22)$. This means there are a total of 462 spatial points. Note that the MDC analysis involves sequentially fitting MDC at various energies, ranging from $E = E_F$ to $E = -0.14$ eV with a step size of 1 meV, resulting in 141 points. Thus, the present spatial spectral analysis was performed over 65000 fittings in total. Subsequently, we performed a statistical and correlation analysis on “parameters,” which consist of the obtained fitting parameters [$I_{\text{MDC}}^{ij}(\omega)$, $\varepsilon_k^{ij}(\omega)$, and $\Delta k^{ij}(\omega)$] as well as the velocities (v_F and v_h) and coupling parameters (λ_{tot} , λ_{ee} , and λ_{eb}) obtained by further analyzing the determined band dispersions

$\varepsilon_k^{ij}(\omega)$. The details of statistical and correlation analysis are described in the following sections.

B. Spatial and statistical evaluation of physical parameters

Figure 2 summarizes our extended spatial spectral analysis, which enabled identifying the spatial distribution of various electronic properties. Specifically, we determined the intensity, position, and width of the MDC peak at E_F (I_{MDC} , k_F , and Δk), as well as band parameters (v_F and v_h), and coupling parameters (λ_{tot} , λ_{ee} , and λ_{eb}). Here, the histogram shows the probability of raw values of each parameter, whereas the spatial distribution of parameters, both in raw and standardized forms, are displayed using blue-green-yellow and (cold color)-white-(warm color) contrasts, respectively. Note that a generally accepted Z-score normalization was employed for

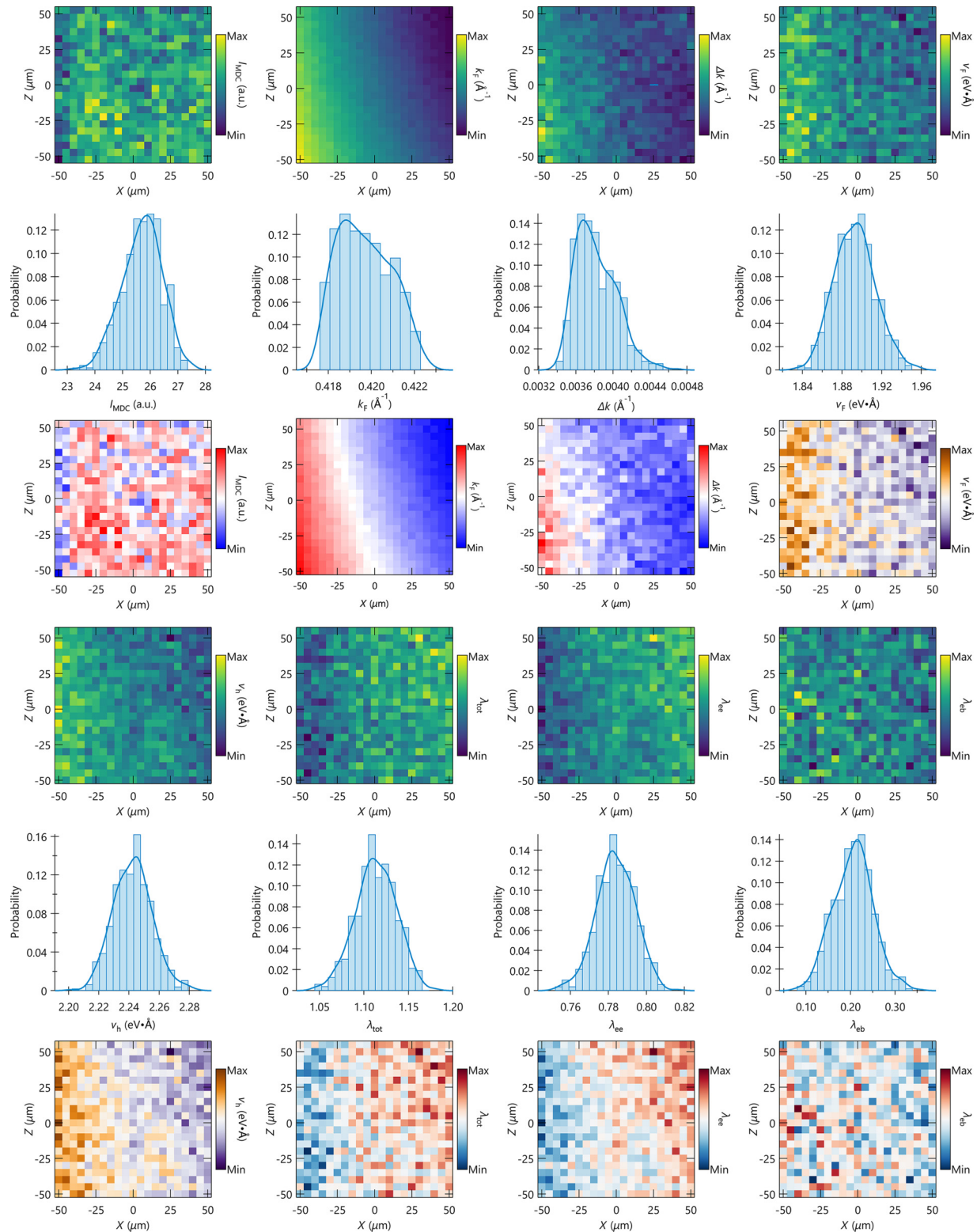


FIG. 2. Spatial and statistical evaluation of band and coupling parameters. Raw spatial distribution, histogram, and standardized spatial distribution of band parameters and coupling parameters: I_{MDC} , k_{F} , Δk , v_{F} , v_{h} , λ_{tot} , λ_{ee} , and λ_{eb} .

standardization. Overall, standardization revealed clear spatial dependencies. In particular, spatial evolution can be easily seen in the case of k_{F} and Δk among the MDC peak parameters, while the distribution of I_{MDC} appears to be rather homogeneous. Additionally, the spatial distribution of other

band and coupling parameters appears to follow the trend observed in k_{F} , which is reasonable considering that they are induced based on the peak position of MDCs.

On the other hand, extrinsic effects, including fitting errors, contact potential difference of the sample [27], local surface

tilting or warping, and misalignment between the manipulator and detector axes, could potentially account for the observed k_F shift. However, we have ruled out all of these possibilities (see Supplemental Material Note 1 and Supplemental Material Figs. 1–5). The fitting errors were notably small owing to the high SN ratio. The work functions exhibited remarkable uniformity within a significantly narrow 95% confidence interval of the Fermi energy, just 0.2 meV across the region of interest on the sample surface. Assuming the observed variations were induced by the local rotational fluctuations on the surface, we evaluated the influence of the surface tilting and warping. However, these factors were insufficient to provide a reasonable explanation for the observed shift in k_F or E_F . Furthermore, we also found that k_F exhibits almost no correlation to E_F , which can serve as an indicator of the above-mentioned surface issues. The misalignment between the manipulator and detector axes can also be excluded because the spatial fluctuations in the peak width Δk are not typically anticipated for a surface with a homogeneous doping level, as assumed when considering no intrinsic k_F shift.

Here, one may notice that the Fermi velocity v_F also shows a small but non-negligible variation, seemingly different from the reported universal behavior of the nodal Fermi velocity in many high- T_c cuprate families with various dopings [28]. Indeed, this can be attributed to the different levels of experimental accuracy. The present mean Fermi velocity was quantified as $v_F = 1.893 \pm 0.02$, with the error determined by the standard deviation. Its range extends to only 6%, which is considerably smaller than the reported universal range defined by the experimental error of 20%.

Figure 2 demonstrates another important aspect, which is the statistical evaluation of physical parameters using spatially resolved ARPES data. The coupling parameters were quantified as follows: $\lambda_{\text{tot}} = 1.11 \pm 0.02$, $\lambda_{\text{ee}} = 0.78 \pm 0.01$, and $\lambda_{\text{eb}} = 0.21 \pm 0.04$, with the errors given by the standard deviations. It is worth noting that our approach enables more reliable quantification of physical parameters compared to conventional methods, where quantification relies on a single spatial point and may result in a deviation from a true value. However, it is important to consider possible sources that may result in the observed spatial dependence. In the present case, the spatial dependence in many parameters is likely linked with the Fermi momentum k_F , which is the fingerprint of the doping level of the system. Hence, the present spatially resolved data set can be regarded as a natural combinatorial system with different doping levels, given the small but finite spatial change in $k_F = 0.420 \pm 0.001 \text{ \AA}^{-1}$. This also demonstrates that the present analysis is suitable and applicable for studying an artificial system, such as a bulk-combinatorial system, in which a large number of different compounds are spatially spread and prepared by a single synthesis [29].

C. Correlation evaluation between physical parameters

Besides the statistical evaluation of the physical parameters, the quantification of physical parameters further provides a useful functionality of spatially resolved ARPES, providing an opportunity to explore the correlation between the physical parameters.

To visualize the correlation between multiple experimentally determined variables, we displayed the pairwise relationships using scatter-plot matrices. Figures 3 and 4 show the scatter-plot matrices for the band parameters and coupling parameters, respectively. In these matrices, the diagonal plots show the distribution of each variable as a histogram, while the off-diagonal plots are the scatter plots showing the correlation between each pair of variables. In the scatter plot, each data point is represented by a point, and the overall pattern of the data points can reveal the strength and direction of the correlation between each pair of variables.

Furthermore, for better visualization and characterization of the correlation between variables, we performed the K -means clustering, which is an unsupervised learning technique and is useful for analyzing the spatially resolved ARPES data [18]. The clustering was performed based on the MDC peak information, including I_{MDC} , k_F , and Δk , which were obtained by the first-step analysis. We note that the k_F and Δk are significant physical quantities that are related to the carrier concentration and scattering rate ($1/l$, where l denotes a mean free path), respectively. Here, we should also address two issues for data processing. The first issue was that the input variables were standardized by the Z -score normalization to obtain reasonable clustering results, and to ensure that each variable was given equal weight, especially when each data set has significantly different variances. The second issue was determining the maximum number of clusters (n_k), a hyper-parameter of the K -means clustering algorithm, for which we set $n_k = 2$. The value was adopted in terms of the sample size needed for statistical evaluation, although the optimal maximum number in the present case was estimated as four from the n_k dependence of the sum of square errors. It should be noted that a simpler correlation analysis without clustering, as well as clustering using larger n_k 's, yielded essentially the same conclusion. Further information on the sample size and the n_k dependence of clustering can be found in Supplemental Material Note 3 and Supplemental Material Figs. 11–16 [22].

Importantly, we found almost the same direction and spread of data points between the two clusters in Figs. 3 and 4, where each of the data points in each cluster is indicated by different colors. This means that the correlation analysis of each cluster yields consistent results. This is interesting because the present results apparently suggest the presence of two domains with different doping levels, as evidenced by the two Gaussian-like distributions in k_F . These findings demonstrate that the combination of correlation and clustering analysis is useful not only for understanding correlation properties, but also for revealing spatially dependent electronic properties that may be hidden within a large data set.

Looking at the correlation properties between band parameters in Fig. 3, it can be easily understood that the peak intensity shows almost no correlation to other parameters, as seen in nearly circular distributions, whereas the other parameters show a positive correlation with each other that rises to the right. In particular, the peak position and width, k_F and Δk , have a closer correlation than the other parameters, as seen in the sharper spread. In contrast, the correlation properties are more complex between band and coupling parameters, as seen in Fig. 4, where various types of correlations appear. At first glance, the perfect negative correlation is outstanding between

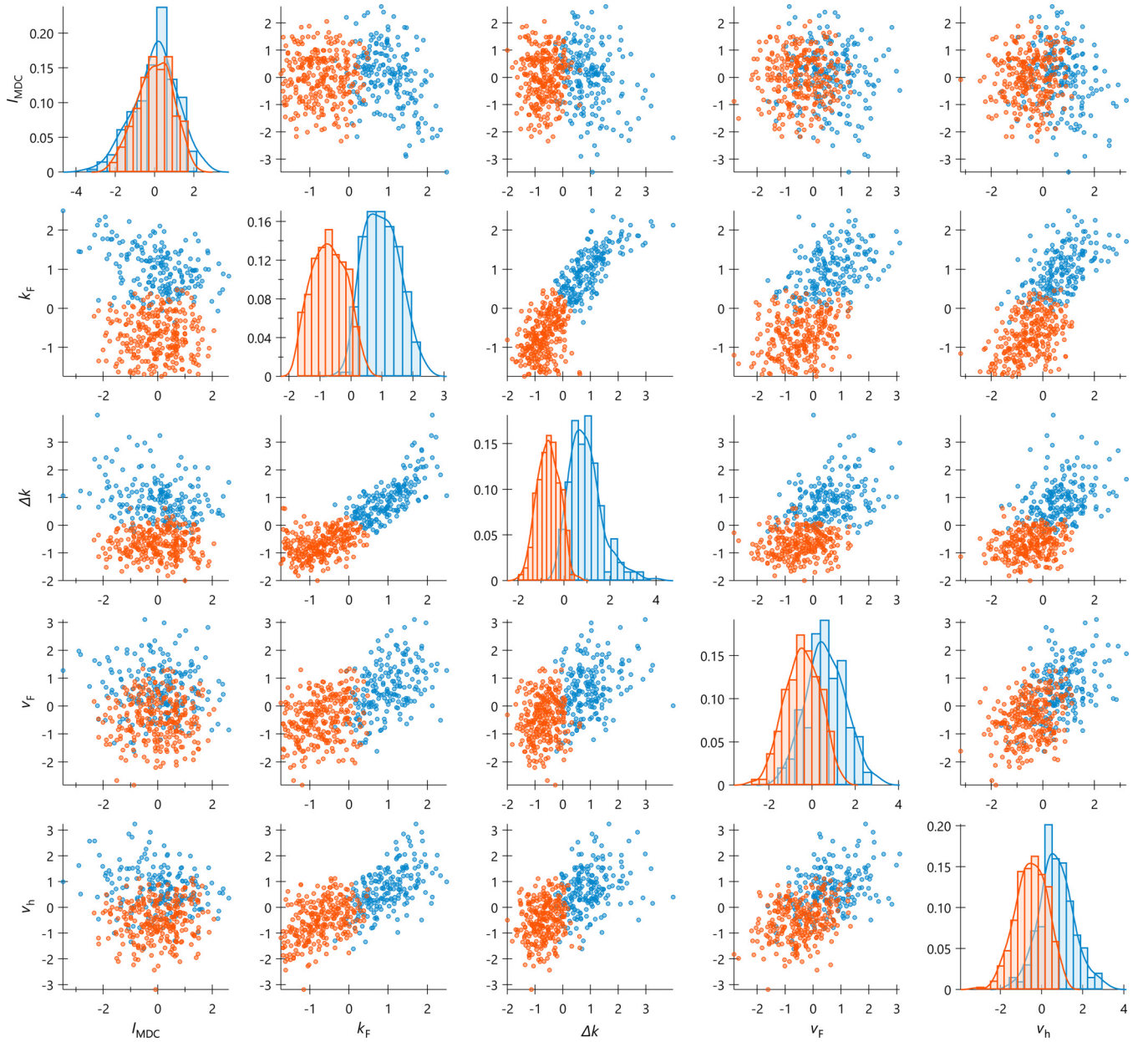


FIG. 3. Scatter-plot matrix for various band parameters. Each off-diagonal plot in the matrix represents the correlation between two variables among the various band parameters, I_{MDC} , k_{F} , Δk , v_{F} , and v_{h} . The diagonal plots show the distribution of each variable through histograms.

v_{F} and λ_{tot} as well as v_{h} and λ_{ee} , as a natural consequence of the derivation of coupling parameters where $\lambda_{\text{tot}} \propto v_{\text{F}}^{-1}$ and $\lambda_{\text{ee}} \propto v_{\text{h}}^{-1}$. Next, the band parameters (k_{F} , v_{F} , and v_{h}), having positive correlations with each other, show negative correlations with the λ_{tot} and λ_{ee} coupling parameters, consistent with the general expectation that a larger coupling to electrons yields a smaller velocity with heavier effective mass. Here, the λ_{tot} and λ_{ee} coupling parameters have the positive correlation and thereby show the same negative correlations to the band parameters. Interestingly, a remaining electron-boson coupling parameter λ_{eb} shows a different correlation to the band parameters; namely, the trends are almost opposite compared with those for λ_{tot} and λ_{ee} . The results imply

that the electron-boson coupling around 70 meV along the nodal direction is insensitive to the small difference in the doping level in the overdoped regime, while λ_{ee} is sensitive. Furthermore, we should emphasize a rather weak but negative correlation between electron-electron and electron-boson coupling parameters λ_{ee} and λ_{eb} . In general, accessing the correlation between the physical parameters is not easy, as it requires systematic measurements using multiple samples. Hence, our present approach has a great advantage in that the correlation between the physical parameters is straightforwardly evaluated from a single sample.

Subsequently, to numerically measure the strength and direction of the correlation between two variables, we calculated

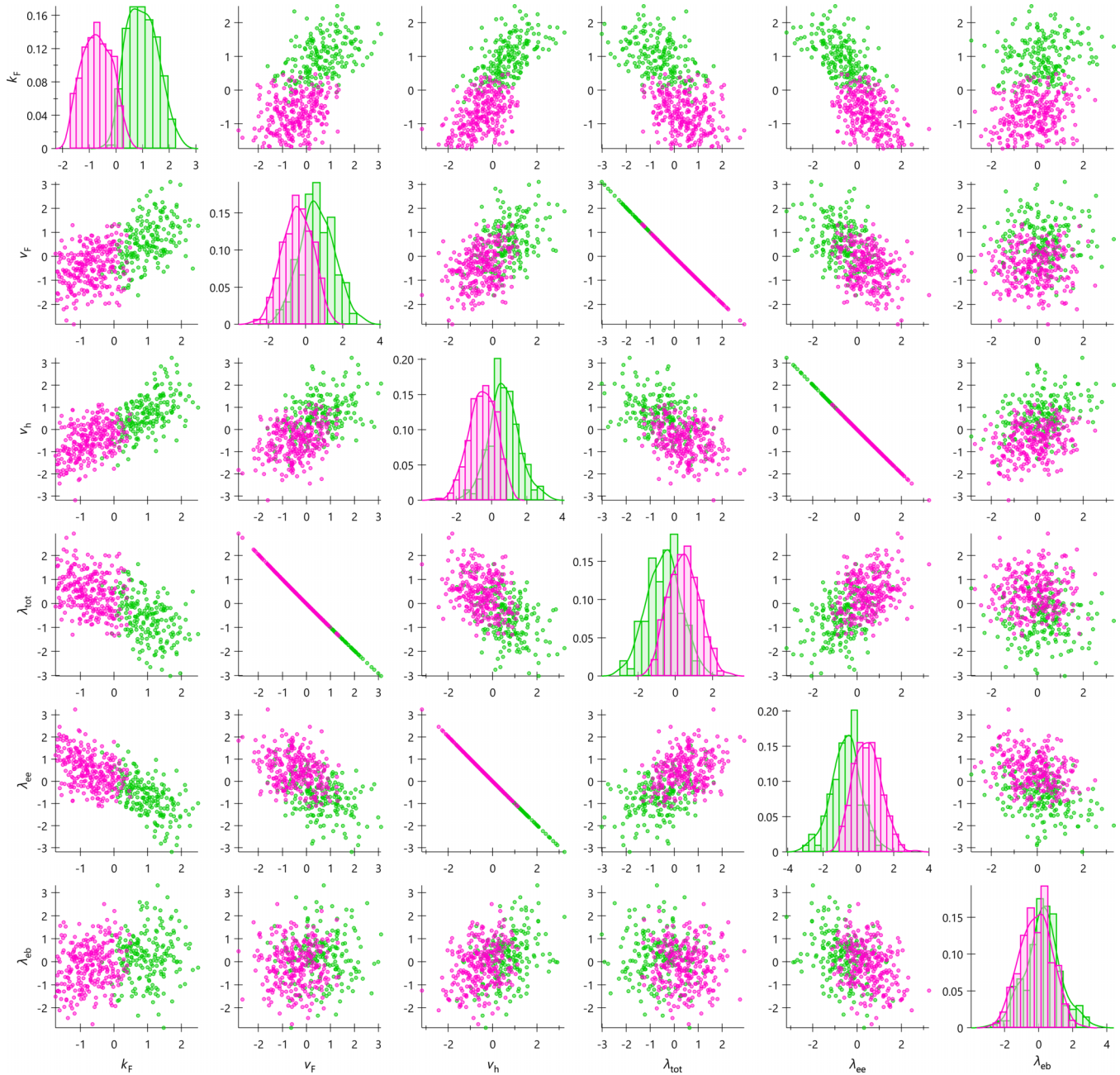


FIG. 4. Scatter-plot matrix for coupling parameters. Each off-diagonal plot in the matrix represents the correlation between two variables among the coupling parameters, λ_{tot} , λ_{ee} , and λ_{eb} , including the selected band parameters, k_F , v_F , and v_h . The diagonal plots show the distribution of each variable through histograms.

the most commonly used, the Pearson correlation coefficient (r) and p value [19]. The explanations of these variables are described in the Methods section. Figure 5 shows the Pearson correlation coefficient and p value obtained for band parameters and coupling parameters within each cluster. We observed that most of the p values are zero, as seen in Figs. 5(c1), 5(c2) and 5(d1), 5(d2), indicating statistical validation of the obtained Pearson correlation coefficient. One may notice that the p value becomes considerably high when the Pearson correlation coefficient approaches zero, which highlights the difficulty of the Pearson correlation coefficient in handling circular or no correlations between variables, as it measures only linear correlations.

While the calculated Pearson correlation coefficients in Fig. 5 follow the qualitative descriptions already mentioned above, we should point out that the cluster's dependence is quantitatively different between the band and coupling parameters. In the case of the band parameters [Figs. 5(a1) and 5(a2)], the Pearson correlation coefficients show the same positive direction but different strengths of the correlation among the parameters except for the I_{MDC} parameter. These results may stem from the differences in the underlying electronic properties of the two domains. Nevertheless, the Pearson correlation coefficients for the coupling parameters are quantitatively consistent between the two clusters [Figs. 5(b1) and 5(b2)]. Therefore, the observed correlations

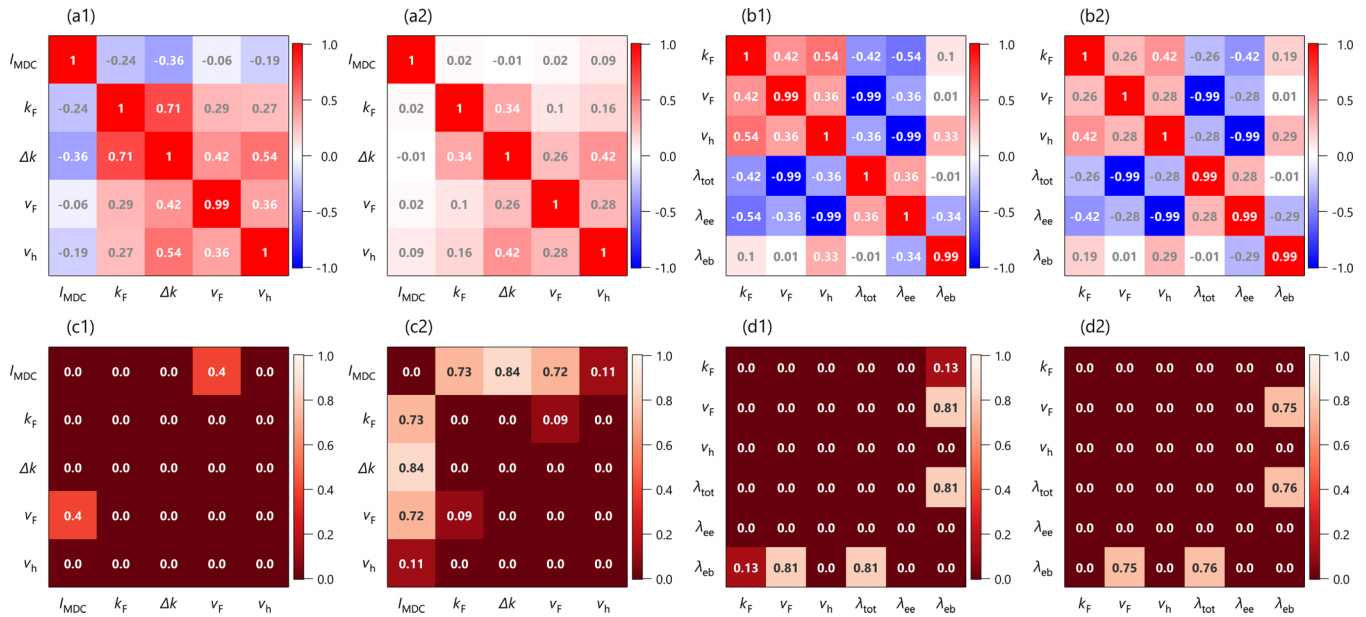


FIG. 5. Pearson correlation coefficients and p values for band and coupling parameters. (a1), (a2) The Pearson correlation coefficients of the band parameters for clusters $k = 1$ and $k = 2$, respectively. (c1), (c2) The p value corresponding to (a1) and (a2), respectively. (b1), (b2) and (d1), (d2) Same as (b1), (b2) and (d1), (d2), respectively, but for coupling parameters.

between the coupling parameters are not the result of experimental noise or analytical error. Instead, they are likely indicative of genuine properties of high- T_c cuprates.

Furthermore, to clarify the correlation between the coupling parameters and the transport properties of high- T_c cuprates, we empirically deduced the hole concentration x . Based on an experimental k_F - x relation reported in a previous ARPES study [30], the doping level was estimated as the overdoping with $x = 0.215 \pm 0.005$, converted from the Fermi momentum k_F (see Supplemental Material Fig. 17 [22]). As demonstrated in Figs. 6(a1) and 6(a2), a smaller k_F corresponds to a larger doping x , which leads to a lower superconducting transition temperature T_c in this doping regime. We then examined the correlation between the coupling parameters and the hole concentration x , as shown in Figs. 6(b1) and 6(b2), where we adopted the correlation analysis without clustering for simplicity. What we found is a clear

positive correlation between the hole concentration x and the electron-electron interaction λ_{ee} in this overdoped regime, with the Pearson correlation coefficient (p value) of $r = 0.71$ ($p = 0.0$). The increase of λ_{ee} is associated with doping while lowering T_c in this doping regime, implying that stronger electron-electron interaction contributes to deforming electron pairing. This tendency is consistent with the reduction of the superfluid density with doping while lowering T_c in the overdoped $\text{La}_{2-x}\text{Sr}_x\text{CuO}_4$, reported via careful measurements of the magnetic penetration depth and the phase stiffness [31].

In contrast, the electron-boson coupling related to the α kink, denoted as λ_{eb}^α , has a weak negative correlation to the hole concentration with $r = -0.25$ and $p = 0.0$. This indicates that the λ_{eb}^α is weakly corproative with T_c in this overdoping regime. However, it is important to note that the interpretation of electron-boson interactions and their interplay requires careful consideration, as there may be multiple

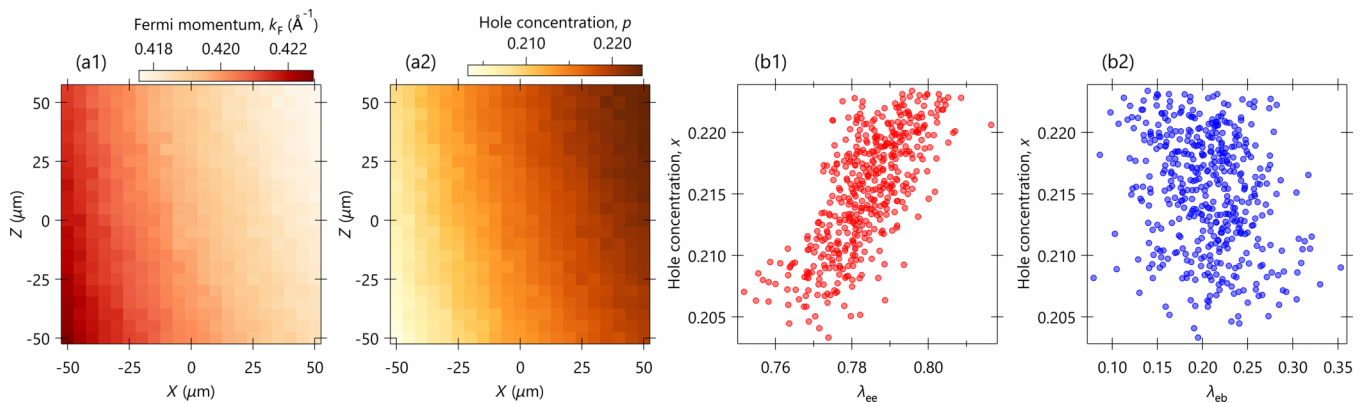


FIG. 6. Correlation between the coupling parameters and hole concentration. (a1), (a2) The spatial distribution of the Fermi momentum k_F and the hole concentration x , respectively. (b1), (b2) The scattering plots between the hole concentration x against the coupling parameters of electron-electron and electron-boson interactions, λ_{ee} and λ_{eb} , respectively.

electron-boson interactions involved with different correlations to the other parameters, such as λ_{ee} and x . For example, a previous ARPES study has suggested a positive correlation between electron-electron and electron-phonon interactions in Bi-based cuprates based on antinodal ARPES spectra [10]. Additionally, momentum-dependent, multiple electron-boson couplings have been reported in Bi2212 [6]. Therefore, a deconvolution of these multiple electron-boson couplings in terms of energy and momentum would be necessary to fully uncover the correlations between electron-boson and electron-electron interactions in high- T_c cuprates, though this is beyond the scope of the current paper.

IV. CONCLUSION

In summary, we extended the detailed spectral analysis to the spatial ARPES mapping data set to establish an approach for understanding the spatial evolution of many-body interactions. The presence and influence of spatial inhomogeneity should be taken into account in order to more precisely quantify many-body interactions, as spatial inhomogeneity is one of the fundamental characteristics of correlated electron systems [32]. Although the advancements in energy and momentum resolutions in previous ARPES experiments have enabled the quantification of many-body interactions [24], the evaluation typically relies on a single spatial point due to the relatively poor spatial resolution, which leads to the integration of spatial information and may introduce accidental errors.

Our spatial-spectral analysis technique has useful functionalities, such as statistical and correlation evaluations of physical parameters. So far, there are few attempts to spatially map the physical parameters [16,33], though the overall spatial evolution might be elusive by tracing spatial changes in a pixel-to-pixel manner. One may wonder if our approach might be unsuitable for clarifying the spatial evolution of physical

parameters, as it implicitly assumes spatial homogeneity for the statistical evaluation. However, by combining the clustering analysis, the spatial evolutions of physical parameters can be evaluated for each classified group. Hence, our spatial-spectral analysis with clustering benefits the rapidly developing research field, such as ARPES on combinatorial systems [29] as well as nano-ARPES in operando [33]. Besides, the statistical and correlation evaluations of physical parameters should provide a higher level of understanding of physical parameters accessed via ARPES. We hope that our approach utilizing the spatially resolved ARPES and machine learning will reveal unknown aspects of electronic interactions and physics in strongly correlated electron systems.

Finally, our technique is fundamentally applicable to many other systems, particularly quantum materials, where microscopic electronic properties play a key role in determining their unique physical properties. Therefore, it is important for future studies to explore and disentangle the complex interplay of many-body interactions, not limited to the present high- T_c cuprate systems but also to other electronic material systems, for a better understanding of their physical properties.

ACKNOWLEDGMENTS

We thank E. F. Schwier, M. Arita, H. Takita, and A. Ino for their support of the ARPES experiments. We also thank Hiroshima Synchrotron Radiation Center (HiSOR) for access to the Laser micro-ARPES system (Proposal No. 14-A-38) that contributed to the results presented here. We express our gratitude to the N-BARD, Hiroshima University, for supplying the liquid helium. This work was supported by the Japan Society for the Promotion of Science (JSPS) KAKENHI Grants No. JP19K03749 and No. JP19H05823, and the JSPS Bilateral Program, Grants No. JPJSBP120209941 and No. JPJSBP120239943, and QST President's Strategic Grant QST Advanced Study Laboratory.

-
- [1] Y. Tokura, N. Kawasaki, and N. Nagaosa, Emergent functions of quantum materials, *Nat. Phys.* **13**, 1056 (2017).
 - [2] B. Keimer, S. A. Kivelson, M. R. Norman, S. Uchida, and J. Zaanen, From quantum matter to high-temperature superconductivity in copper oxides, *Nature (London)* **518**, 179 (2015).
 - [3] A. Lanzara *et al.*, Evidence for ubiquitous strong electron-phonon coupling in high-temperature superconductors, *Nature (London)* **412**, 510 (2001).
 - [4] J. Lee *et al.*, Interplay of electron-lattice interactions and superconductivity in $\text{Bi}_2\text{Sr}_2\text{CaCu}_2\text{O}_{8+\delta}$, *Nature (London)* **442**, 546 (2006).
 - [5] H. Iwasawa *et al.*, Isotopic fingerprint of electron-phonon coupling in high- T_c cuprates, *Phys. Rev. Lett.* **101**, 157005 (2008).
 - [6] H. Anzai, M. Arita, H. Namatame, M. Taniguchi, M. Ishikado, K. Fujita, S. Ishida, S. Uchida, and A. Ino, A new landscape of multiple dispersion kinks in a high- T_c cuprate superconductor, *Sci. Rep.* **7**, 4830 (2017).
 - [7] O. Rösch and O. Gunnarsson, Electron-phonon interaction in the t-J model, *Phys. Rev. Lett.* **92**, 146403 (2004).
 - [8] Z. P. Yin, A. Kutepov, and G. Kotliar, Correlation-Enhanced electron-phonon coupling: applications of GW and screened hybrid functional to bismuthates, chloronitrides, and other high- T_c superconductors, *Phys. Rev. X* **3**, 021011 (2013).
 - [9] S. Gerber *et al.*, Femtosecond electron-phonon lock-in by photoemission and x-ray free-electron laser, *Science* **357**, 71 (2017).
 - [10] Y. He *et al.*, Rapid change of superconductivity and electron-phonon coupling through critical doping in Bi-2212, *Science* **362**, 62 (2018).
 - [11] S. Johnston, F. Vernay, B. Moritz, Z.-X. Shen, N. Nagaosa, J. Zaanen, and T. P. Devereaux, Systematic study of electron-phonon coupling to oxygen modes across the cuprates, *Phys. Rev. B* **82**, 064513 (2010).
 - [12] J. Lee *et al.*, Interfacial mode coupling as the origin of the enhancement of T_c in FeSe films on SrTiO_3 , *Nature (London)* **515**, 245 (2014).
 - [13] F. Schrodli, F. Cheenicode Kabeer, A. Aperis, and P. M. Oppeneer, Exploring multichannel superconductivity in ThFeAsN , *Phys. Rev. B* **104**, 094516 (2021).

- [14] J. Bardeen, L. Cooper, and J. R. Schrieffer, Theory of superconductivity, *Phys. Rev.* **108**, 1175 (1957).
- [15] H. Eisaki, N. Kaneko, D. Feng, A. Damascelli, P. Mang, K. Shen, Z.-X. Shen, and M. Greven, Effect of chemical inhomogeneity in bismuth-based copper oxide superconductors, *Phys. Rev. B* **69**, 064512 (2004).
- [16] H. Iwasawa, E. F. Schwier, M. Arita, A. Ino, H. Namatame, M. Taniguchi, Y. Aiura, and K. Shimada, Development of laser-based scanning μ -ARPES system with ultimate energy and momentum resolutions, *Ultramicroscopy* **182**, 85 (2017).
- [17] E. Jones, T. Oliphant, and P. Peterson, SciPy: Open source scientific tools for Python, (2001) [Online]. Available: <http://www.scipy.org/>.
- [18] H. Iwasawa, T. Ueno, T. Masui, and S. Tajima, Unsupervised clustering for identifying spatial inhomogeneity on local electronic structures, *npj Quantum Mater.* **7**, 24 (2022).
- [19] B. M. Ayyub and R. H. McCuen, *Probability, Statistics, and Reliability for Engineers and Scientists* (CRC Press, Boca Raton, 2011).
- [20] A. Mans *et al.*, Experimental proof of a structural origin for the shadow fermi surface of $\text{Bi}_2\text{Sr}_2\text{CaCu}_2\text{O}_{8+\delta}$, *Phys. Rev. Lett.* **96**, 107007 (2006).
- [21] H. Anzai, A. Ino, M. Arita, H. Namatame, M. Taniguchi, M. Ishikado, K. Fujita, S. Ishida, and S. Uchida, Relation between the nodal and antinodal gap and critical temperature in superconducting $\text{Bi}2212$, *Nat. Commun.* **4**, 1815 (2013).
- [22] See Supplemental Material at <http://link.aps.org/supplemental/10.1103/PhysRevResearch.5.043266> for discussions on extrinsic experimental factors, bare band, and clustering analysis, which includes Ref. [34], as well as the relationship between the Fermi momentum and doping level.
- [23] A. A. Kordyuk, S. V. Borisenko, A. Koitzsch, J. Fink, M. Knupfer, and H. Berger, Bare electron dispersion from experiment: Self-consistent self-energy analysis of photoemission data, *Phys. Rev. B* **71**, 214513 (2005).
- [24] H. Iwasawa, High-resolution angle-resolved photoemission spectroscopy and microscopy, *Electron. Struct.* **2**, 043001 (2020).
- [25] W. Zhang *et al.*, Identification of a new form of electron coupling in the $\text{Bi}_2\text{Sr}_2\text{CaCu}_2\text{O}_8$ superconductor by laser-based angle-resolved photoemission spectroscopy, *Phys. Rev. Lett.* **100**, 107002 (2008).
- [26] J. D. Rameau, H.-B. Yang, G. D. Gu, and P. D. Johnson, Coupling of low-energy electrons in the optimally doped $\text{Bi}_2\text{Sr}_2\text{CaCu}_2\text{O}_{8+\delta}$ superconductor to an optical phonon mode, *Phys. Rev. B* **80**, 184513 (2009).
- [27] A. Fero, C. L. Smallwood, G. Affeldt, and A. Lanzara, Impact of work function induced electric fields on laser-based angle-resolved photoemission spectroscopy, *J. Electron Spectrosc. Relat. Phenom.* **195**, 237 (2014).
- [28] X. J. Zhou *et al.*, Universal nodal Fermi velocity, *Nature (London)* **423**, 398 (2003).
- [29] I. Hase, A. Iyo, Y. Higashi, T. Yanagisawa, and K. Kawashima, Bulk-combinatorial method for exploring new superconductors and its mathematical aspect, *J. Phys.: Conf. Ser.* **2323**, 012009 (2022).
- [30] Y.-G. Zhong *et al.*, Continuous doping of a cuprate surface: Insights from in situ angle-resolved photoemission, *Phys. Rev. B* **98**, 140507(R) (2018).
- [31] I. Božović, X. He, J. Wu, and A. T. Bollinger, Dependence of the critical temperature in overdoped copper oxides on superfluid density, *Nature (London)* **536**, 309 (2016).
- [32] E. Dagotto, Complexity in strongly correlated electronic systems, *Science* **309**, 257 (2005).
- [33] P. Hofmann, Accessing the spectral function of in operando devices by angle-resolved photoemission spectroscopy, *AVS Quantum Sci.* **3**, 021101 (2021).
- [34] S. B. Hulley, S. R. Cumming, W. S. Browner, D. Grady, and T. B. Newman, *Designing Clinical Research: An Epidemiologic Approach*, 4th ed. (Lippincott Williams & Wilkins, Philadelphia, PA, 2013).